APL Materials

RESEARCH ARTICLE | NOVEMBER 03 2023

Tuning the band topology of GdSb by epitaxial strain

Special Collection: Emerging Materials in Antiferromagnetic Spintronics

Hadass S. Inbar; Dai Q. Ho; Shouvik Chatterjee; Aaron N. Engel; Shoaib Khalid; Connor P. Dempsey; Mihir Pendharkar; Yu Hao Chang; Shinichi Nishihaya; Alexei V. Fedorov; Donghui Lu; Makoto Hashimoto; Dan Read; Anderson Janotti; Christopher J. Palmstrøm

APL Mater. 11, 111106 (2023)
https://doi.org/10.1063/5.0155218

View Online

Export Citation

CrossMark

07 November 2023 07:54:06

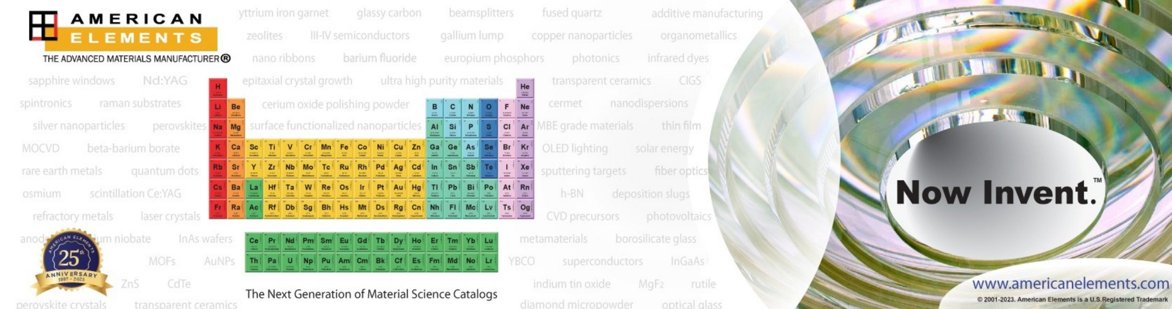

APL Materials ARTICLE pubs.aip.org/aip/apm

Tuning the band topology of GdSb by epitaxial strain

Cite as: APL Mater. 11, 111106 (2023); doi: 10.1063/5.0155218
Submitted: 18 April 2023 • Accepted: 10 October 2023 •
Published Online: 3 November 2023

Hadass S. Inbar,[1,a)] Dai Q. Ho,[2,3] Shouvik Chatterjee,[4,b)] Aaron N. Engel,[1] Shoaib Khalid,[5,c)] Connor P. Dempsey,[4] Mihir Pendharkar,[4,d)] Yu Hao Chang,[1] Shinichi Nishihaya,[1,e)] Alexei V. Fedorov,[6] Donghui Lu,[7] Makoto Hashimoto,[7] Dan Read,[4,8] Anderson Janotti,[2] and Christopher J. Palmstrøm[1,4,a)]

AFFILIATIONS

[1] Materials Department, University of California Santa Barbara, Santa Barbara, California 93106, USA
[2] Department of Materials Science and Engineering, University of Delaware, Newark, Delaware 19716, USA
[3] Faculty of Natural Sciences, Quy Nhon University, Quy Nhon 59000, Vietnam
[4] Electrical and Computer Engineering Department, University of California Santa Barbara, Santa Barbara, California 93106, USA
[5] Department of Physics, School of Natural Sciences, National University of Science and Technology, Islamabad 44000, Pakistan
[6] Advanced Light Source, Lawrence Berkeley National Laboratory, Berkeley, California 94720, USA
[7] Stanford Synchrotron Radiation Lightsource, SLAC National Accelerator Laboratory, Menlo Park, California 94025, USA
[8] School of Physics and Astronomy, Cardiff University, Cardiff CF24 3AA, United Kingdom

Note: This paper is part of the Special Topic on Emerging Materials in Antiferromagnetic Spintronics.
[a)] **Authors to whom correspondence should be addressed:** hadass@ucsb.edu and cjpalm@ucsb.edu
[b)] **Present address:** Department of Condensed Matter Physics and Materials Science, Tata Institute of Fundamental Research, Mumbai 400005, India.
[c)] **Present address:** Princeton Plasma Physics Laboratory, Princeton, New Jersey 08540, USA.
[d)] **Present address:** Department of Materials Science and Engineering, Stanford University, Stanford, CA 94305, USA.
[e)] **Present address:** Department of Physics, Tokyo Institute of Technology, Tokyo 152-8551, Japan.

ABSTRACT

Rare-earth monopnictide (RE-V) semimetal crystals subjected to hydrostatic pressure have shown interesting trends in magnetoresistance, magnetic ordering, and superconductivity, with theory predicting pressure-induced band inversion. Yet, thus far, there have been no direct experimental reports of interchanged band order in RE-Vs due to strain. This work studies the evolution of band topology in biaxially strained GdSb(001) epitaxial films using angle-resolved photoemission spectroscopy (ARPES) and density functional theory (DFT). As biaxial strain is tuned from tensile to compressive strain, the gap between the hole and the electron bands dispersed along [001] decreases. The conduction and valence band shifts seen in DFT and ARPES measurements are explained by a tight-binding model that accounts for the orbital symmetry of each band. Finally, we discuss the effect of biaxial strain on carrier compensation and magnetic ordering temperature.

© 2023 Author(s). All article content, except where otherwise noted, is licensed under a Creative Commons Attribution (CC BY) license (http://creativecommons.org/licenses/by/4.0/). https://doi.org/10.1063/5.0155218

I. INTRODUCTION

Strain engineering of low-dimensional topological quantum materials serves as a powerful approach to manipulating electronic band structures, thereby controlling topological phase transitions and transport behavior.[1] For example, strained HgTe quantum wells grown in the tensile and compressive regimes were shown to transition from a semimetallic to a two-dimensional topological insulator (TI) system, respectively.[2] Despite the promise of topological state tuning, strain studies of quantum materials as thin films are typically restricted to local, defect-induced strain gradients[3–5] or to strain levels below 1% strain[6,7] in the case of uniform strain in lattice-mismatched growths. In TIs such as the group V-chalcogenides (X_2Z_3, X = Bi, Sb and Z = Te, Se), unstrained growths occur even on substrates with high lattice mismatch due to the weak bonding between the van der Waals layers.[8,9] In addition to the

07 November 2023 07:54:06

challenge of stabilizing highly strained pseudomorphic topological materials, visualizing band structure modifications as a function of strain/pressure has been difficult in both bulk single crystals and thin films. In single crystals, large pressure cells are difficult to implement, and when using mechanical strain tuning apparatus, special care is needed to ensure the application of uniform strain.[10–13] For thin films, there are limited reports combining strained film growth with direct spectroscopic tools, such as angle-resolved photoemission spectroscopy (ARPES), with a few exceptions in oxide films.[14,15]

Recent reports of bulk rare-earth monopnictide (RE-V) crystals under hydrostatic pressure reveal the emergence of a superconducting phase transition in nonmagnetic RE-Vs,[16–18] and theoretical predictions suggest potential strain and pressure-induced transitions in band topology.[19–23] In addition to observing a strain-driven topological phase transition in the RE-V system, strain studies of RE-Vs are highly relevant for spintronic-based applications as another control knob to tune magnetoresistance and magnetic ordering in RE-V thin films. Finally, coupled with III–V semiconductors, RE-V thin films and particles have shown many potential device applications,[24] including buried metallic contacts,[25] THz emitters and detectors,[26,27] thermoelectrics,[28,29] plasmonic heterostructures,[30] and diffusion barriers.[31] Therefore, straining RE-V thin films and thickness tuning present another avenue to control the functional properties of these magnetic semimetals, specifically by modifying magnetic exchange interactions and the charge carrier ratio in these otherwise electron–hole-compensated semimetal systems.

Here, we use ARPES to study the evolution of the electronic structure of GdSb thin films grown by molecular beam epitaxy (MBE) subjected to 2% tensile (+2%) and 2% compressive (−2%) biaxial strain. GdSb belongs to the RE-V family of compounds and is particularly interesting due to the relatively small electron–hole band energy gap that can be inverted via attainable strain/hydrostatic pressure, resulting in a nontrivial Z_2 topological invariant classification.[19] We demonstrate the ability to tune the bandgap and Néel temperature (T_N) in strained GdSb thin films and thereby control the topological phase transition from a trivial to a nontrivial state. GdSb thin films also present high magnetoresistance,[32] have a type-II antiferromagnetic ordering at nearly the highest temperature of all RE-V (T_N = 24 K),[33] and can be epitaxially integrated with III–V semiconductors[34] [see Figs. 1(a)–1(c)]. This approach to band engineering via epitaxial strain can be broadly applied to a wide range of RE-V antiferromagnet semimetals.

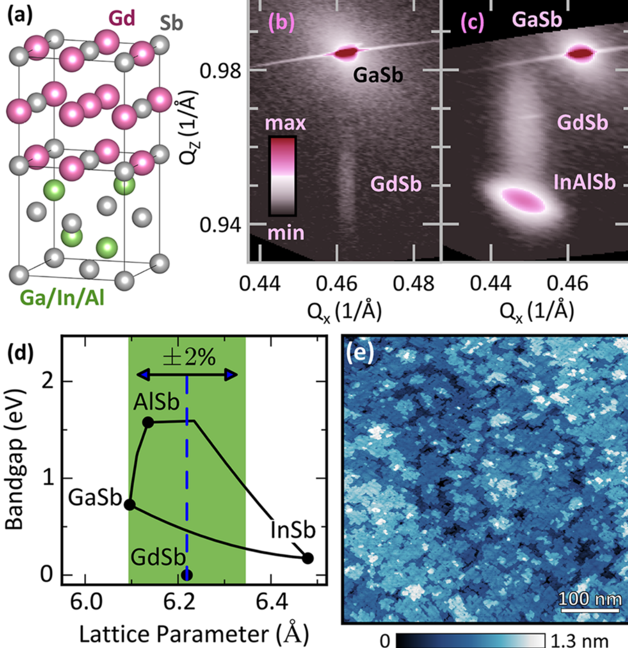

FIG. 1. (a) Crystal structure and epitaxial relationship of the rocksalt GdSb/zincblende III–V (001) orientation. RSM of the (226) reflection in (b) −2% and (c) +2% strained GdSb films, demonstrating coherent growth to the underlying III–V layer. (d) Biaxial strain window of GdSb and range of III–V bandgaps and lattice parameters used for buffer layer growth. (e) STM image of the −2% strained film: 4 nm GdSb/GaSb(001) (V = −0.5 V, I = 1 nA).

II. MATERIALS AND METHODS

GdSb has a lattice parameter of a = 6.219 Å between InSb (6.479 Å) and GaSb (6.096 Å)/AlSb (6.136 Å), allowing high tensile and compressive biaxial strain by varying the underlying semiconducting III–V buffer layer structure, as shown in Fig. 1(d). MBE was used to grow epitaxial GdSb(001) thin films on $In_xGa_{1-x}Sb/In_xAl_{1-x}Sb$ buffer layers nucleated on a GaSb(001) substrate. For photoemission and scanning tunneling microscopy (STM) studies, p-type doped substrates and p-type $In_xGa_{1-x}Sb$ buffer layers were used. By changing the Ga/In or Al/In concentration in the buffer layer, the in-plane lattice parameter was adjusted before GdSb growth, as shown in Fig. 1(d). For magneto-transport measurements, undoped $In_xAl_{1-x}Sb$ buffer layers and epi-ready undoped GaSb(001) wafers (Wafer Technology Ltd.) were used. Further details on the GdSb growth window, ARPES measurement conditions, and electronic characterization of lattice-matched unstrained films are detailed in our previous report.[32] The growth of strained films was studied *in situ* with reflection high-energy electron diffraction, STM, and confirmed *ex situ* with x-ray diffraction reciprocal space map (RSM) measurements. Grazing incidence RSM of (226) reflections for 4 nm-thick GdSb films are shown in Figs. 1(b) and 1(c), confirming that the layers remain pseudomorphically strained to the buffer layer. *In situ* STM scans of the 2% compressive strained GdSb film grown directly on GaSb in Fig. 1(e) and on metamorphic III–V buffer layers[32] confirm the growth of a smooth and continuous GdSb film with terrace step heights consistent with half of a unit cell. We investigated the electronic structure of GdSb theoretically using density functional theory (DFT) and the screened hybrid functional of Heyd, Scuseria, and Ernzerhof (HSE06)[35,36] with 25% of exact exchange and accounting for spin–orbit coupling, as implemented in the Vienna *ab initio* Simulation Package (VASP) code.[37,38] See the supplementary material for additional details on MBE growth, ARPES measurements, and DFT calculations.

III. RESULTS AND DISCUSSION

The Fermi surface of GdSb is composed of two hole pockets (β, δ) at the Brillouin zone center (Γ), a third spin–orbit split-off band (γ) positioned below the Fermi level, and three ellipsoidal

07 November 2023 07:54:06

© Author(s) 2023

electron pockets (α) at the Brillouin zone edge (X_1, X_2, X_3, the X_3 high-symmetry point transforming to the Z point in the tetragonal $I4/mmm$ space group under biaxial strain) [see Fig. 2]. In Figs. 2–4, we monitor the band topology evolution under strain and address the effect of finite thickness quantization on the additional subbands observed in ARPES and modeled with DFT. DFT-calculated and ARPES-extracted Fermi wave vectors and band extrema positions for both strain values are summarized in Table I.

Figures 2(a)–2(d) highlight the ARPES high-symmetry cuts studied for the electron pockets located at $X_{1,2}$ points in the film plane. Due to the high k_z broadening expected for the vacuum ultraviolet light used in the ARPES measurements,[39] the scans of the electron pocket in Fig. 2(d) present both the minor and major axes of the ellipsoidal electron pocket, the latter projecting from the neighboring Brillouin zone in Figs. 2(a) and 2(b). ARPES of the electron pockets at $X_{1,2}$ [Figs. 2(a)–2(d)] shows an increase in the bandwidth and major axis Fermi wave vector upon compressive strain, with the band minima shifting from $\alpha_{X_{1,2}}^{+2\%} = -0.375$ eV to $\alpha_{X_{1,2}}^{-2\%} = -0.440$ eV. The hole band extrema in the film plane remain largely unchanged: $\delta_{X_{1,2}}^{+2\%} = -0.66$ eV, $\beta_{X_{1,2}}^{+2\%} = -1.41$ eV and $\delta_{X_{1,2}}^{-2\%} = -0.68$ eV, $\beta_{X_{1,2}}^{-2\%} = -1.45$ eV (see valence band pockets in Fig. 4 and summary of DFT and fit values in Table I). These relatively small changes in the bands lying in the film-plane agree with our DFT calculations in Fig. 2(g), which predict only a small shift in the electron pockets at $X_{1,2}$ as a function of biaxial strain.

Figures 2(e) and 2(f) show the electron pocket at the Z high-symmetry point, positioned along the film plane normal. Figure 3 depicts the expanded momentum range of the E–k cuts in Figs. 2(e) and 2(f), capturing electron and hole pockets lying perpendicular to the film plane (Z for $k_\parallel = 0$) and in the film plane ($X_{1,2}$ high-symmetry points from neighboring Brillouin zones projecting to $\overline{M}$ at $k_\parallel = \frac{2\pi}{a}$). Fitting the electron and hole bands at Z along $W-Z-W$ in [Figs. 2(f) and 3], we see a downward shift in the electron pocket from $\alpha_Z^{+2\%} = -0.34$ eV to $\alpha_Z^{-2\%} = -0.41$ eV and for the valence bands an upward shift: $\delta_Z^{+2\%} = -0.9$ eV to $\delta_Z^{-2\%} = -0.59$ eV and $\beta_Z^{+2\%} = -1.45$ eV to $\beta_Z^{-2\%} = -1.31$ eV. The influence of epitaxial strain on the hole bands, primarily at

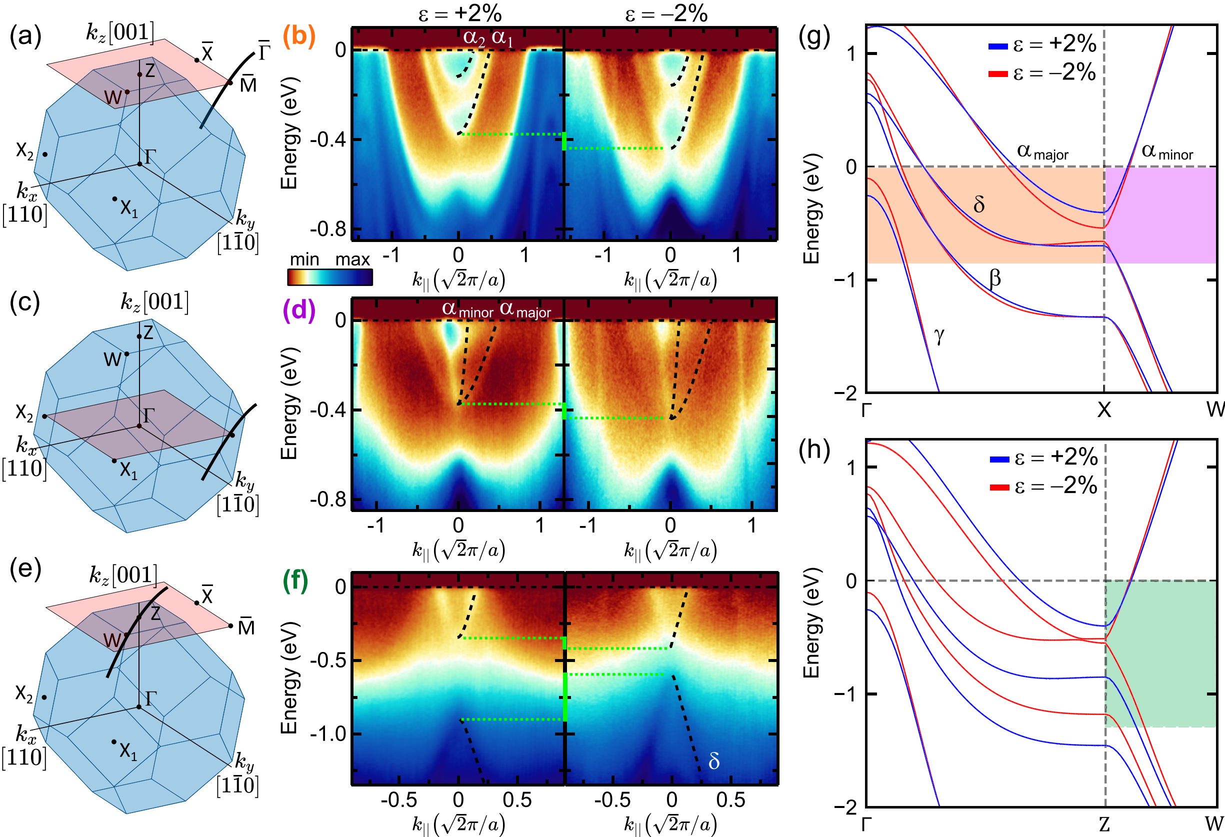

FIG. 2. Band dispersion of electron and hole bands in GdSb films studied with ARPES and strain-induced modifications for $\varepsilon = +2\%$ tensile (left) and $\varepsilon = -2\%$ compressive (right) biaxial strain. (a), (c), and (e) Schematics of the bulk Brillouin zone projected to the (001) surface Brillouin zone, showing the measured k_z plane (pink square) and E–k spectra directions (black line). $\overline{\Gamma}-\overline{M}-\overline{\Gamma}$ cut along the in-plane electron pockets $X_{1,2}$ for (a) and (b) semimajor axis ($\Gamma-X_1-\Gamma$) measured at $k_z = Z$ with a photon energy of 94 eV and (c) and (d) semiminor axis ($W-X_2-W$) measured at $k_z = \Gamma$ with a photon energy of 60 eV. (e) and (f) $\overline{M}-\overline{\Gamma}-\overline{M}$ cuts of the out-of-plane electron pocket semiminor axis ($W-Z-W$) measured at $k_z = Z$ with a photon energy of 88 eV. Black dotted lines are hyperbolic fits to the band dispersions, and the green dotted lines highlight the band shifts. See Table I for the Fermi wave vectors and band extrema extracted from the fits. (g) and (h) DFT-calculated band structures for $\varepsilon = +2, -2\%$ along (g) the in-plane high-symmetry points and (h) film plane normal direction. Fermi levels were set at 0. Shaded regions in (g) and (h) highlight the E–k cuts in panels (b), (d), and (f).

07 November 2023 07:54:06

© Author(s) 2023

TABLE I. Fermi surface of 4 nm-thick strained GdSb(001) films. Band maximum/minimum energy positions, Fermi wave vectors (k_F) for all bands, and the carrier density ratio, obtained from ARPES measurements and DFT calculations. Band extrema are reported for all quantum well subbands observed via ARPES.

			+2% (tensile strain)		−2% (compressive strain)	
			ARPES	DFT	ARPES	DFT
$k_F^{\alpha}(\text{Å}^{-1})$	Minor $W - X$	$X_{1,2}$	0.085 (±0.02)	0.103	0.084 (±0.02)	0.110
		Z	0.11 (±0.05)	0.108	0.089 (±0.02)	0.103
	Major $\Gamma - X$	$X_{1,2}$	0.356 (±0.02)	0.374	0.371 (±0.03)	0.423
		Z	NA	0.364	NA	0.434
α band extrema (eV)		$X_{1,2}$	α_1: −0.375 (±0.004) α_2: −0.118 (±0.006)	−0.405	α_1: −0.440 (±0.004) α_2: −0.157 (±0.004)	−0.540
		Z	−0.34 (±0.02)	−0.398	−0.41 (±0.02)	−0.512
$k_F^{\delta}(\text{Å}^{-1})$	$\overline{M} - \overline{\Gamma} - \overline{M}$		0.230 (±0.030)	0.238	0.184 (±0.030)	0.248
	$\overline{X} - \overline{\Gamma} - \overline{X}$		0.123 (±0.01)	0.175	0.124 (±0.018)	0.189
$k_F^{\beta}(\text{Å}^{-1})$	$\overline{M} - \overline{\Gamma} - \overline{M}$		0.116 (±0.017)	0.127	0.105 (±0.005)	0.151
	$\overline{X} - \overline{\Gamma} - \overline{X}$		0.064 (±0.008)	0.127	0.077 (±0.010)	0.151
γ band extrema (eV)		Γ	−0.32 (±0.01)	−0.255	−0.30 (±0.01)	−0.102
		$X_{1,2}$	−3.205 (±0.05)	−3.33	−3.12 (±0.05)	−3.27
δ band extrema (eV)		$X_{1,2}$	δ_1: −0.66 (±0.02) δ_2: −0.82 (±0.02) δ_3: −1.09 (±0.02)	−0.70	δ_1: −0.68 (±0.02) δ_2: −0.88 (±0.05) δ_3: −1.21 (±0.02)	−0.66
		Z	δ_1: −0.90 (±0.02)	−0.855	δ_1: −0.59 (±0.08)	−0.55
β band extrema (eV)		$X_{1,2}$	β_1: −1.41 (±0.01) β_2: −1.62 (±0.03)	−1.33	β_1: −1.45 (±0.03) β_2: −1.70 (±0.05)	−1.33
		Z	β_1: −1.45 (±0.02)	−1.45	β_1: −1.28 (±0.02)	−1.18
E_g		$X_{1,2}$	0.285 (±0.02)	0.295	0.24 (±0.02)	0.12
		Z	0.56 (±0.03)	0.457	0.18 (±0.08)	−0.04
n_e/n_h			1.52	1.09	1.85	1.11

Z (and only small shifts for the bands dispersing in-plane along $\Gamma - X - W$), agrees with our calculations in Figs. 2(g) and 2(h) and earlier DFT calculations performed for LaSb.[40]

Our DFT calculations in Figs. 2(g) and 2(h) show that at $\varepsilon = -2\%$, GdSb transitions into a topological semimetal state as the hole and electron bands anti-cross along $\Gamma - Z$ and are inverted at Z. In contrast, the in-plane electron and hole bands at $X_{1,2}$ remain gapped. Due to high k_z broadening in Figs. 2(e), 2(f), and 3, the valence band pockets at $k_z = \Gamma$ also project to the $k_z = Z$ plane, leading to a blurred background intensity preventing the observation of the expected topological surface states (TSS) for the compressively strained film (TSS in RE-Vs typically have a weaker spectral intensity compared to the bulk bands[41,42]), and leading to a larger error bar in our estimation of electron band minima at Z. Further work using bulk-sensitive soft x-ray (SX) ARPES would enable better ability to resolve the bulk band dispersion along $\Gamma - Z$. Nevertheless, the ARPES dispersions for the hole bands at X and Z and the electron bands lying in the film plane are consistent with our DFT calculations and support the predicted bandgap reduction scenario at Z moving from tensile to compressive strain.

Table I summarizes the experimental and calculated bandgaps at X and Z for each strain level, $E_{gX/Z} = \alpha_{X/Z} - \delta_{X/Z}$, and shows qualitative agreement. The reduced bandgap when transitioning from tensile to compressive strain suggests two possible scenarios for $\varepsilon = -2\%$: inverted bands with a nontrivial topology or uninverted bands with a smaller trivial gap. The gap measured for the compressive strained film is closer to that of unstrained GdSb films[32] (with a 20 nm thickness) $E_{gX}^{0\%} = E_{gZ}^{0\%} = \alpha_X^{0\%} - \delta_X^{0\%} = 0.21$ eV. Compared to the thicker unstrained film, quantum confinement effects in the thinner 4 nm thick strained films are expected to be stronger in the in-plane electron pockets (X) and negligible in the out-of-plane pocket (Z)[43] as demonstrated in our DFT calculation in Fig. S2. Therefore, the close values of $E_{gZ}^{0\%}, E_{gZ}^{-2\%}$ suggest that a transition past the critical bandgap closing point is possible under compressive strain. In order to unequivocally determine a nontrivial band topology in compressive strained GdSb, future work should examine additional strain levels between 0% and −2% biaxial strain to track the gap closing, as well as apply strain beyond $\varepsilon = -2\%$ to access a larger inverted gap. We expect that by further optimizing growth conditions, higher compressive strain

07 November 2023 07:54:06

© Author(s) 2023

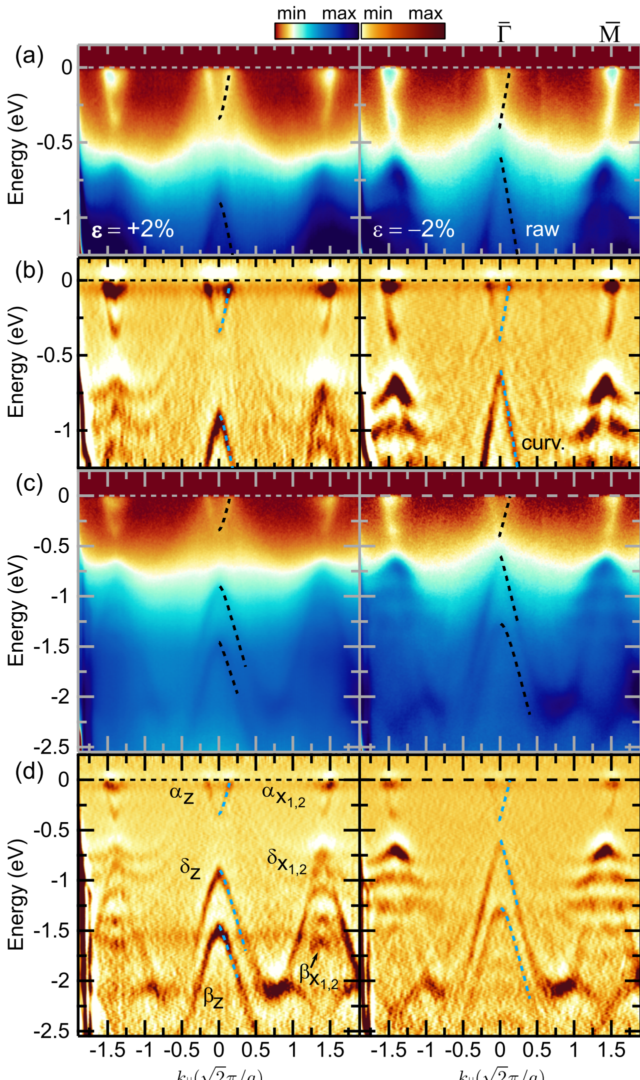

FIG. 3. *E*–*k* dispersion along $\overline{M}-\overline{\Gamma}-\overline{M}$ ($X_{1,2}-W-Z-W-X_{1,2}$) in biaxial strained GdSb films measured with a photon energy of 88 eV, an expanded range of the cuts shown in Figs. 2(e) and 2(f). (a) and (c) Raw data and (b) and (d) curvature plots of the raw data presenting the band dispersions (a) and (b) near the Fermi level and (c) and (d) over a wider energy range including the β hole pocket maximum.

should also be possible, for example, by growing directly on InAs, $\varepsilon = -2.5\%$.

We have further checked the predicted topological nature of the strained GdSb by evaluating the Z_2 strong topological index ν_0 according to the band parity product criteria[44] considered at eight time-reversal inversion momenta (TRIM) points: Γ, 4 L, 2 X, and Z, where $(-1)^{\nu_0} = \prod_{i=1}^{8} \delta_i$, with δ_i being the parity product at each TRIM point for all occupied bands. Time-reversal symmetry (Θ) and primitive-lattice translation symmetry ($T_{1/2}$) in GdSb are broken; however, their combination is preserved ($S = \Theta T_{1/2}$), enabling the classification of the topological nature using the Z_2 topological invariant.[45] In the unstrained and tensile cases, the Z_2 invariant $\nu_0 = 0$, demonstrating a trivial topological state. In contrast, we observe a change in the parity product at the Z point (from + to −) in the compressively strained case, resulting in a Z_2 index $\nu_0 = 1$, which indicates a nontrivial topological band structure. We have found that there are only minor changes in our DFT calculation between the room-temperature lattice parameter (6.219 Å) and low-temperature/DFT relaxed GdSb lattice parameter (6.197 Å), with band extrema changes smaller than 50 meV. We used the calculated equilibrium lattice parameter of 6.197 Å for unstrained GdSb to consistently determine the Poisson ratio (see further details in the supplementary material, Sec. I). However, since the calculated inverted gap for the 2% compressive layer is 40 meV, it can be sensitive to the starting relaxed lattice parameter used. In our earlier work, we showed that HSE06 AFM calculations for unstrained GdSb accurately describe the electronic bandgap at the bulk X point compared to other DFT functionals.[32] Thus, the 2% compressive GdSb appears to lie within the transition region between a strong topological insulator with a nonzero value of the strong topological invariant and a Z_2 trivial topological state.

In RE-Vs under hydrostatic pressure,[19,21] all three $\Gamma - X$ high-symmetry directions are equivalent, yet epitaxial strain primarily affects bands in the direction normal to the film plane, i.e., along [001] ($\Gamma - Z$). The bandgap changes in $\Gamma - Z$ can be explained using a simple tight-binding (TB) model, accounting for the orbital composition of the electron and hole bands near the Fermi level and the scaling of nearest-neighbor and next-nearest neighbor interactions with strain (see Fig. 5 and the supplementary material for details on the TB model). Based on the orbital-resolved DFT electronic band structure in Fig. 5(a), we construct a TB model that reproduces well the DFT-calculated band structure and the effect of strain on hopping terms (Table S1). The band structure of GdSb resulting from our TB parametrization is presented in Figs. 5(d) and S1 over a narrow and wide energy range, respectively. From Fig. 5(a), it is apparent that the out-of-plane electron pocket centered at Z is mainly composed of Gd d_{xy} orbitals, which form $dd\sigma$-like bonds in the [110] direction and $dd\pi$-like bonds along the [101] direction [highlighted in Fig. 5(b), with $dd\delta$ hopping being negligible, i.e., close to 0]. The heavy-(δ) and light-(β) hole bands consist of Sb $p_x + p_y$ orbitals along $\Gamma - Z$, forming three different hopping terms $t_{1,2} = pp\pi \pm pp\sigma$ $t_3 = pp\pi$. The split-off valence band (γ) is made up of p_z orbitals. Moreover, p–d mixing in GdSb through $pd\sigma$ and $pd\pi$ bond formation is necessary to describe the sharp conduction and valence band dispersions along $Z - W$. Similarly, the in-plane electron pockets at X_1/X_2 and δ hole band dispersions along the $\Gamma - X_{1,2}$ axis are composed of Gd d_{yz}/d_{xz} orbitals and Sb $p_y + p_z/p_x + p_z$ orbitals, respectively.

The DFT-calculated gap at Z, $E_g(Z)$, between the conduction and valence bands as a function of strain level is shown in Fig. 5(c). Compressive strain widens the bandwidth along $X - W$ and $Z - W$ for the hole and electron pockets [see Table I and Figs. 2(g) and 2(h)]. Upon applying compressive strain, the orbital overlap increases between the in-plane hopping terms of the $p_x\, p_y\, d_{xy}$ orbitals, leading to increased dispersion in both the valence and the conduction bands. However, because the d orbital hopping terms have a stronger distance dependence than the p orbitals,[46] shown in Fig. 5(c), the electron pocket has a more significant increase in its bandwidth moving from tensile to compressive strain. This behavior

07 November 2023 07:54:06

© Author(s) 2023

also explains the topological phase transition trend observed for RE-Vs due to lanthanide contraction.[19,22] Lighter lanthanide elements have both larger ionic radius[47] and larger unit cells,[48] yet overall the ratio of the lanthanide ionic radius to the RE-V unit cell increases for the lighter lanthanides, leading to higher *d*–*d* orbital overlap eventually resulting in band inversion, despite the decrease in *p*–*p* orbital overlap.

Strain-induced band inversion along $\Gamma - Z$ in Figs. 2(h) and 3 is reproduced in the TB model in Fig. 5(d) and explains the more substantial modifications observed in ARPES and calculated in DFT for band dispersions composed of atomic orbitals distributed within the film plane. For the in-plane electron pockets at $X_{1,2}$ under compressive strain, the *d*–*d* orbital overlap in the (011)/(101) faces is affected by both the reduced distance along [010]/[100] and the slightly expanded out-of-plane lattice parameter along [001]. However, due to the small Poisson ratio of GdSb, the total distance between the d_{xz}/d_{yz} orbitals decreases, leading to a slight reduction of the gap at $X_{1,2}$. In conclusion, the TB model demonstrates the importance of both Gd–Gd $dd\sigma$ and Sb–Sb $pp\pi$ bonding in determining the degree of band inversion at the *Z* high-symmetry point.

Next, we map the quantum well states in the conduction and valence bands. Two electron subband pockets are present at both strain levels in Fig. 2(b). Scans of the hole pockets along $\overline{M} - \overline{\Gamma} - \overline{M}$ ($X_{1,2} - \Gamma - X_{1,2}$ in the bulk Brillouin zone) and $\overline{X} - \overline{\Gamma} - \overline{X}$ ($K - \Gamma - K$ in the bulk Brillouin zone) in Fig. 4 show multiple quantum well states and agree with the number of subbands seen in our DFT calculations in Fig. S2 for films of the same thickness. The same number of quantum well subbands and similar energy splitting for the biaxially strained films confirm the growth of atomically uniform films of the same thickness and comparable interface potentials when grown on GaSb ($\varepsilon = -2\%$) and $In_{0.65}Ga_{0.35}Sb$ ($\varepsilon = +2\%$) buffer layers.

Due to quantum size effects, the band extrema positions in the 4 nm-thick films (detailed in Table I) are expected to be shifted down (up) [i.e., to higher (lower) binding energies] for the in-plane dispersing hole (electron) pockets at $X_{1,2}$ compared to the DFT calculations in Fig. 2(g) performed for bulk-like GdSb. DFT calculations in Fig. S1 (see the supplementary material), modeling the effect of quantum confinement in 13 ML of GdSb(001) slabs, show that the electron pockets in the film plane at $X_{1,2}$ are experiencing quantum confinement, in contrast to the electron bands lying at *Z*, which follow the bulk band-structure behavior. Therefore, pockets in the direction normal to the film plane are less susceptible to quantum confinement in the (001) plane due to their in-plane orbital composition.[43]

A modest change in the concentration of all charge carriers is seen as a function of strain (see our earlier work[32] for details on the carrier density analysis). Overall, the charge carrier ratio increases with compressive strain from $\left(\frac{n_e}{n_h}\right)_{+2\%} = 1.52$ to $\left(\frac{n_e}{n_h}\right)_{-2\%} = 1.85$, suggesting that biaxial strain could serve as another degree of freedom to tune magnetoresistance in RE-Vs. As in past observations for LuSb[49] (a nonmagnetic RE-V analog), due to quantum confinement effects in the 4 nm-thick films, the Fermi surface area of the hole pockets and the electron pockets in the strained thin films is slightly

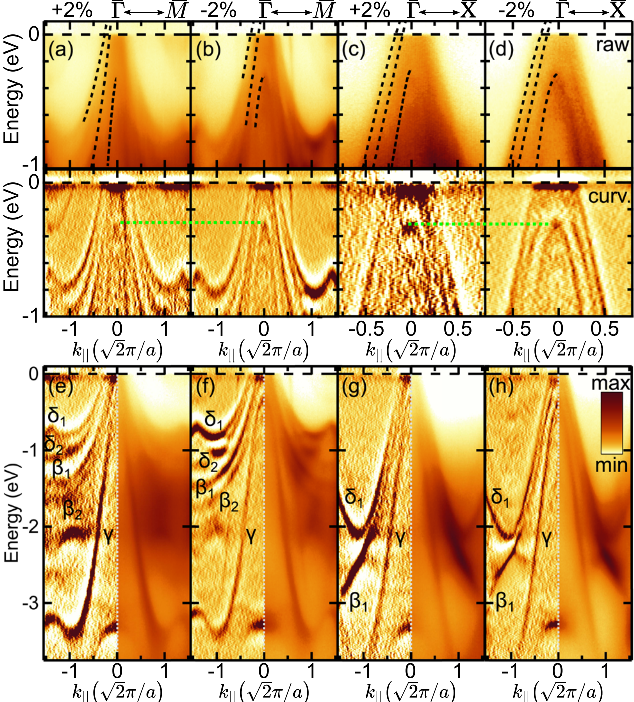

FIG. 4. *E*–*k* dispersion of hole pockets in biaxial strained GdSb films measured at $k_z = \Gamma$ (photon energy of 60 eV). (a)–(d) ARPES spectra near the Fermi level. The green dotted line highlights the same γ valence band maximum position, and the black lines show overlaid fits along (a) and (b) $\overline{M} - \overline{\Gamma} - \overline{M}$ and (c) and (d) $\overline{X} - \overline{\Gamma} - \overline{X}$. Top panel: raw data, bottom panel: curvature plots of the raw data. (e)–(h) Wider energy range of the same cuts in (a)–(d), showing the quantum well states. The plots on the right-hand side present the raw data, and the plots on the left-hand side display the curvature plot. Fermi wave vectors extracted from the fits to the valence band and band extrema in panels (e)–(h) are detailed in Table I.

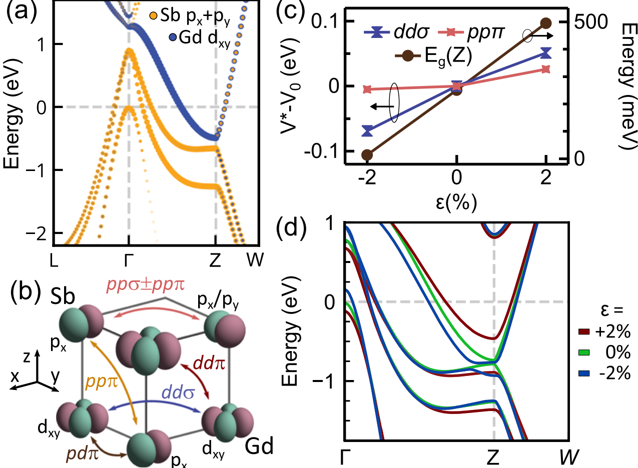

FIG. 5. Strain effect on orbital overlap in GdSb. (a) Nonmagnetic DFT calculations of the electronic band structure in GdSb and the orbital character of the DFT wavefunctions. (b) Illustration of relevant atomic orbitals and primary interaction paths at the *Z* point. (c) Tight binding hopping term decay rate with increasing strain (see the supplementary material for details) and the evolution of the calculated gap at the TRIM *Z* point vs strain. (d) Tight binding band structure of GdSb and its dependence on strain level.

07 November 2023 07:54:06

© Author(s) 2023

smaller than the values extracted via ARPES for thicker unstrained GdSb films.[32] The electron-rich carrier ratio measured for both thin films, deviating from exact compensation in unstrained bulk GdSb, agrees with our earlier studies of quantum confinement effects in RE-Vs.[49]

Finally, we address the effect of strain on the magnetic properties of GdSb. Due to the absence of orbital angular momentum in the $4f^7$ configuration of the Gd^{3+} ion, GdSb represents an ideal isotropic Heisenberg model system for studying magnetic exchange interactions. GdSb can be considered a parent compound of the half-Heusler structure GdPtV (V = Bi, Sb), which shows complex behavior, such as an antiferromagnetic to ferromagnetic transition in GdPtSb due to strain gradients[5] and chiral anomaly and anisotropic magnetotransport in the predicted Weyl semimetal GdPtBi.[50] The Néel temperature (T_N) in the thin films is inferred from the kink in the resistivity temperature dependence, similar to features previously reported in GdSb bulk single crystals[51–53] and RE-V thin films.[54] A 2.6 K increase in T_N from +2% tensile (24.3 K) to −2% compressive (26.9 K) strained films is observed in Fig. S3. Based on our TB model, a reduction in the lattice parameter results in increased p–d orbital hopping, which, in turn, leads to a higher T_N (see further details in the supplementary material). To our knowledge, this is the first study showing the direct impact of epitaxial strain on superexchange p–d hopping in a RE-V and could guide future efforts in strain tuning the magnetic ordering temperature of other materials beyond the RE-V family. Building on these results, the effect of strain/pressure in other RE-Vs with more complex magnetic behavior, such as Ce-V[55] and Eu-VI,[56] can be modeled or applied to semiconducting RE-V nitrides, such as ScN[57] and GdN.[58]

IV. CONCLUSIONS

In summary, we have followed with ARPES and DFT the evolution of the bulk band structure in biaxial strained GdSb quantum wells and demonstrated the tuning of bandgaps in RE-Vs through epitaxial strain. We report the successful growth of strained GdSb films integrated with a conventional III–V semiconducting substrate, and the resulting trends in magnetic ordering temperature and charge carrier ratios are discussed. The synthesis of high-quality epitaxial GdSb is an important step toward practical control of transport characteristics in magnetic Weyl semimetals. Our TB model based on nearest and next-nearest neighbor interactions describes well the electronic structure of GdSb. We have shown that biaxial compressive strain is expected to promote d–d hopping in the rare earth t_{2g} conduction bands to a larger extent than the pnictogen p band hopping, resulting in band inversion and a higher electron carrier density. This work opens the door to future studies of strain-controlled topological phase transitions and semimetal-semiconductor transitions in RE-Vs[43] and RE-V derived compounds, such as topological half-Heusler alloys (RE-Pt/Pd-V).[59–61]

SUPPLEMENTARY MATERIAL

See the supplementary material for additional details on ARPES surface preparation, DFT calculations, ARPES- and DFT-extracted Fermi wave vectors and band extrema, confinement effects, tight binding model construction, and magnetic properties of strained GdSb films.

ACKNOWLEDGMENTS

Synthesis of thin films, development of a prototype ultra-high vacuum suitcase, ARPES experiments, and theoretical work were supported by the U.S. Department of Energy (Contract No. DE-SC0014388). Development of the growth facilities and low-temperature magnetotransport measurements were supported by the Office of Naval Research through the Vannevar Bush Faculty Fellowship under Award No. N00014-15-1-2845. Scanning probe studies were supported by the NSF (Award No. DMR-1507875). This research used resources of the Advanced Light Source (spin-resolved ARPES beamline 10.0.1.2), which is a DOE Office of Science User Facility under Contract No. DE-AC02-05CH11231. Use of the Stanford Synchrotron Radiation Lightsource, SLAC National Accelerator Laboratory (beamline 5-2), is supported by the U.S. Department of Energy, Office of Science, Office of Basic Energy Sciences, under Contract No. DE-AC02-76SF00515. We acknowledge the use of shared facilities of the NSF Materials Research Science and Engineering Center (MRSEC) at the University of California Santa Barbara (Grant No. DMR-2308708). DFT calculations used the National Energy Research Scientific Computing Center (NERSC), a U.S. Department of Energy Office of Science User Facility operated under Contract No. DE-AC02-05CH11231. H.S.I. gratefully acknowledges support from the UC Santa Barbara NSF Quantum Foundry funded via the Q-AMASE-i program under Award No. DMR-1906325 and support for further developments of the vacuum suitcases. A.J. and D.Q.H. acknowledge support from the NSF through the University of Delaware Materials Research Science and Engineering Center (Grant No. DMR-2011824).

07 November 2023 07:54:06

AUTHOR DECLARATIONS

Conflict of Interest

The authors have no conflicts to disclose.

Author Contributions

H.S.I. and D.Q.H. contributed equally to this work.

H.S.I. and C.J.P. conceived the study. Thin film growth, x-ray diffraction, and transport measurements were performed by H.S.I. with assistance from S.C., C.P.D., and M.P. ARPES measurements were performed by H.S.I. with assistance from S.C., A.N.E., Y.H.C., S.N., D.R., A.V.F., D.L., and M.H. and analyzed by H.S.I. DFT calculations were performed by D.Q.H. with assistance from S.K. and A.J. supervising. H.S.I. and D.Q.H. constructed the tight-binding model. S.C., A.N.E., C.P.D., and M.P. designed ultra-high vacuum components and sample holders. The manuscript was prepared by H.S.I., D.Q.H., A.J., and C.J.P. C.J.P. supervised the experimental work. All authors discussed the results and commented on the manuscript.

Hadass S. Inbar: Conceptualization (equal); Formal analysis (equal); Investigation (equal); Methodology (equal); Writing – original draft (equal); Writing – review & editing (equal). **Dai Q. Ho**: Formal analysis (equal); Investigation (equal); Writing – original draft (equal);

© Author(s) 2023

Writing – review & editing (equal). **Shouvik Chatterjee**: Formal analysis (equal); Investigation (equal); Writing – review & editing (equal). **Aaron N. Engel**: Methodology (equal); Writing – review & editing (equal). **Shoaib Khalid**: Methodology (equal); Writing – review & editing (equal). **Connor P. Dempsey**: Methodology (equal); Writing – review & editing (equal). **Mihir Pendharkar**: Methodology (equal); Writing – review & editing (equal). **Yu Hao Chang**: Methodology (equal); Writing – review & editing (equal). **Shinichi Nishihaya**: Methodology (equal); Writing – review & editing (equal). **Alexei V. Fedorov**: Resources (equal); Writing – review & editing (equal). **Donghui Lu**: Resources (equal); Writing – review & editing (equal). **Makoto Hashimoto**: Resources (equal); Writing – review & editing (equal). **Dan Read**: Methodology (equal); Writing – review & editing (equal). **Anderson Janotti**: Funding acquisition (equal); Investigation (equal); Methodology (equal); Supervision (lead); Writing – review & editing (equal). **Christopher J. Palmstrøm**: Conceptualization (equal); Funding acquisition (equal); Investigation (equal); Methodology (equal); Supervision (equal); Writing – review & editing (equal).

DATA AVAILABILITY

The data that support the findings of this study are available from the corresponding authors upon reasonable request.

REFERENCES

[1] J. M. Kim, M. F. Haque, E. Y. Hsieh, S. M. Nahid, I. Zarin, K. Jeong, J. So, H. Park, and S. Nam, Adv. Mater. **35**, 2107362 (2022).
[2] P. Leubner, L. Lunczer, C. Brüne, H. Buhmann, and L. W. Molenkamp, Phys. Rev. Lett. **117**, 086403 (2016).
[3] D. Walkup, B. A. Assaf, K. L. Scipioni, R. Sankar, F. Chou, G. Chang, H. Lin, I. Zeljkovic, and V. Madhavan, Nat. Commun. **9**, 1550 (2018).
[4] A. K. Nayak, J. Reiner, R. Queiroz, H. Fu, C. Shekhar, B. Yan, C. Felser, N. Avraham, and H. Beidenkopf, Sci. Adv. **5**, 37 (2019).
[5] D. Du, S. Manzo, C. Zhang, V. Saraswat, K. T. Genser, K. M. Rabe, P. M. Voyles, M. S. Arnold, and J. K. Kawasaki, Nat. Commun. **12**, 2494 (2021).
[6] A. Barfuss, L. Dudy, M. R. Scholz, H. Roth, P. Höpfner, C. Blumenstein, G. Landolt, J. H. Dil, N. C. Plumb, M. Radovic, A. Bostwick, E. Rotenberg, A. Fleszar, G. Bihlmayer, D. Wortmann, G. Li, W. Hanke, R. Claessen, and J. Schäfer, Phys. Rev. Lett. **111**, 157205 (2013).
[7] G. N. Phan, K. Nakayama, K. Sugawara, T. Sato, T. Urata, Y. Tanabe, K. Tanigaki, F. Nabeshima, Y. Imai, A. Maeda, and T. Takahashi, Phys. Rev. B **95**, 224507 (2017).
[8] L. A. Walsh and C. L. Hinkle, Appl. Mater. Today **9**, 504 (2017).
[9] M. Brahlek, J. Lapano, and J. S. Lee, J. Appl. Phys. **128**, 210902 (2020).
[10] D. Flötotto, Y. Bai, Y. H. Chan, P. Chen, X. Wang, P. Rossi, C. Z. Xu, C. Zhang, J. A. Hlevyack, J. D. Denlinger, H. Hong, M. Y. Chou, E. J. Mittemeijer, J. N. Eckstein, and T. C. Chiang, Nano Lett. **18**, 5628 (2018).
[11] S. Riccò, M. Kim, A. Tamai, S. McKeown Walker, F. Y. Bruno, I. Cucchi, E. Cappelli, C. Besnard, T. K. Kim, P. Dudin, M. Hoesch, M. J. Gutmann, A. Georges, R. S. Perry, and F. Baumberger, Nat. Commun. **9**, 4535 (2018).
[12] V. Sunko, E. Abarca Morales, I. Marković, M. E. Barber, D. Milosavljević, F. Mazzola, D. A. Sokolov, N. Kikugawa, C. Cacho, P. Dudin, H. Rosner, C. W. Hicks, P. D. C. King, and A. P. Mackenzie, Npj Quantum Mater. **4**, 46 (2019).
[13] C. Lin, M. Ochi, R. Noguchi, K. Kuroda, M. Sakoda, A. Nomura, M. Tsubota, P. Zhang, C. Bareille, K. Kurokawa, Y. Arai, K. Kawaguchi, H. Tanaka, K. Yaji, A. Harasawa, M. Hashimoto, D. Lu, S. Shin, R. Arita, S. Tanda, and T. Kondo, Nat. Mater. **20**, 1093 (2021).
[14] B. Burganov, C. Adamo, A. Mulder, M. Uchida, P. D. C. King, J. W. Harter, D. E. Shai, A. S. Gibbs, A. P. Mackenzie, R. Uecker, M. Bruetzam, M. R. Beasley, C. J. Fennie, D. G. Schlom, and K. M. Shen, Phys. Rev. Lett. **116**, 197003 (2016).
[15] J. P. Ruf, H. Paik, N. J. Schreiber, H. P. Nair, L. Miao, J. K. Kawasaki, J. N. Nelson, B. D. Faeth, Y. Lee, B. H. Goodge, B. Pamuk, C. J. Fennie, L. F. Kourkoutis, D. G. Schlom, and K. M. Shen, Nat. Commun. **12**, 59 (2021).
[16] F. F. Tafti, M. S. Torikachvili, R. L. Stillwell, B. Baer, E. Stavrou, S. T. Weir, Y. K. Vohra, H.-Y. Yang, E. F. McDonnell, S. K. Kushwaha, Q. D. Gibson, R. J. Cava, and J. R. Jeffries, Phys. Rev. B **95**, 014507 (2017).
[17] C. Q. Xu, B. Li, M. R. van Delft, W. H. Jiao, W. Zhou, B. Qian, N. D. Zhigadlo, D. Qian, R. Sankar, N. E. Hussey, and X. Xu, Phys. Rev. B **99**, 024110 (2019).
[18] M. Zhang, X. Wang, A. Rahman, R. Dai, Z. Wang, and Z. Zhang, Phys. Rev. B **101**, 064106 (2020).
[19] X. Duan, F. Wu, J. Chen, P. Zhang, Y. Liu, H. Yuan, and C. Cao, Commun. Phys. **1**, 71 (2018).
[20] H. Inoue, M. Han, M. Hu, T. Suzuki, J. Liu, and J. G. Checkelsky, Phys. Rev. Mater. **3**, 101202 (2019).
[21] S. Khalid, F. P. Sabino, and A. Janotti, Phys. Rev. B **98**, 220102 (2018).
[22] P. Li, Z. Wu, F. Wu, C. Cao, C. Guo, Y. Wu, Y. Liu, Z. Sun, C.-M. Cheng, D.-S. Lin, F. Steglich, H. Yuan, T.-C. Chiang, and Y. Liu, Phys. Rev. B **98**, 085103 (2018).
[23] J. Kim, H.-S. Kim, and D. Vanderbilt, Phys. Rev. B **98**, 155122 (2018).
[24] C. C. Bomberger, M. R. Lewis, L. R. Vanderhoef, M. F. Doty, and J. M. O. Zide, J. Vac. Sci. Technol. B **35**, 030801 (2017).
[25] T. Sands, C. J. Palmstrøm, J. P. Harbison, V. G. Keramidas, N. Tabatabaie, T. L. Cheeks, R. Ramesh, and Y. Silberberg, Mater. Sci. Rep. **5**, 99 (1990).
[26] C. Kadow, S. B. Fleischer, J. P. Ibbetson, J. E. Bowers, A. C. Gossard, J. W. Dong, and C. J. Palmstrøm, Appl. Phys. Lett. **75**, 3548 (1999).
[27] J. F. O'Hara, J. M. O. Zide, A. C. Gossard, A. J. Taylor, and R. D. Averitt, Appl. Phys. Lett. **88**, 251119 (2006).
[28] W. Kim, J. Zide, A. Gossard, D. Klenov, S. Stemmer, A. Shakouri, and A. Majumdar, Phys. Rev. Lett. **96**, 045901 (2006).
[29] H. Lu, P. G. Burke, A. C. Gossard, G. Zeng, A. T. Ramu, J.-H. Bahk, and J. E. Bowers, Adv. Mater. **23**, 2377 (2011).
[30] E. M. Krivoy, A. P. Vasudev, S. Rahimi, R. A. Synowicki, K. M. McNicholas, D. J. Ironside, R. Salas, G. Kelp, D. Jung, H. P. Nair, G. Shvets, D. Akinwande, M. L. Lee, M. L. Brongersma, and S. R. Bank, ACS Photonics **5**, 3051 (2018).
[31] B. D. Schultz, H. H. Farrell, M. M. R. Evans, K. Lüdge, and C. J. Palmstrøm, J. Vac. Sci. Technol. B **20**, 1600 (2002).
[32] H. S. Inbar, D. Q. Ho, S. Chatterjee, M. Pendharkar, A. N. Engel, J. T. Dong, S. Khalid, Y. H. Chang, T. Guo, A. V. Fedorov, D. Lu, M. Hashimoto, D. Read, A. Janotti, and C. J. Palmstrøm, Phys. Rev. Mater. **6**, L121201 (2022).
[33] D. X. Li, Y. Haga, H. Shida, T. Suzuki, Y. S. Kwon, and G. Kido, J. Phys.: Condens. Matter **9**, 10777 (1997).
[34] C. J. Palmstrøm, Annu. Rev. Mater. Sci. **25**, 389 (1995).
[35] J. Heyd, G. E. Scuseria, and M. Ernzerhof, J. Chem. Phys. **118**, 8207 (2003).
[36] J. Heyd, G. E. Scuseria, and M. Ernzerhof, J. Chem. Phys. **124**, 219906 (2006).
[37] G. Kresse and J. Hafner, Phys. Rev. B **47**, 558 (1993).
[38] G. Kresse and J. Hafner, Phys. Rev. B **49**, 14251 (1994).
[39] K. Kuroda, M. Ochi, H. S. Suzuki, M. Hirayama, M. Nakayama, R. Noguchi, C. Bareille, S. Akebi, S. Kunisada, T. Muro, M. D. Watson, H. Kitazawa, Y. Haga, T. K. Kim, M. Hoesch, S. Shin, R. Arita, and T. Kondo, Phys. Rev. Lett. **120**, 086402 (2018).
[40] S. Khalid and A. Janotti, Phys. Rev. B **102**, 035151 (2020).
[41] T. J. Nummy, J. A. Waugh, S. P. Parham, Q. Liu, H.-Y. Yang, H. Li, X. Zhou, N. C. Plumb, F. F. Tafti, and D. S. Dessau, Npj Quantum Mater. **3**, 24 (2018).
[42] J. Jiang, N. B. M. Schröter, S.-C. Wu, N. Kumar, C. Shekhar, H. Peng, X. Xu, C. Chen, H. F. Yang, C.-C. Hwang, S.-K. Mo, C. Felser, B. H. Yan, Z. K. Liu, L. X. Yang, and Y. L. Chen, Phys. Rev. Mater. **2**, 024201 (2018).
[43] D. Q. Ho, R. Hu, D. Q. To, G. W. Bryant, and A. Janotti, ACS Nano (published online 2023).
[44] L. Fu and C. L. Kane, Phys. Rev. B **76**, 045302 (2007).
[45] R. S. K. Mong, A. M. Essin, and J. E. Moore, Phys. Rev. B **81**, 245209 (2010).

07 November 2023 07:54:06

© Author(s) 2023

[46]W. A. Harrison, *Electronic Structure and the Properties of Solids: The Physics of the Chemical Bond* (Dover Publications, 2012).
[47]Y. Q. Jia, J. Solid State Chem. **95**, 184 (1991).
[48]M. N. Abdusalyamova, H. S. Shokirov, and O. I. Rakhmatov, J. Less-Common Met. **166**, 221 (1990).
[49]S. Chatterjee, S. Khalid, H. S. Inbar, A. Goswami, T. Guo, Y.-H. Chang, E. Young, A. V. Fedorov, D. Read, A. Janotti, and C. J. Palmstrøm, Sci. Adv. **7**, eabe8971 (2021).
[50]C. Schindler, S. Galeski, W. Schnelle, R. Wawrzyńczak, W. Abdel-Haq, S. N. Guin, J. Kroder, N. Kumar, C. Fu, H. Borrmann, C. Shekhar, C. Felser, T. Meng, A. G. Grushin, Y. Zhang, Y. Sun, and J. Gooth, Phys. Rev. B **101**, 125119 (2020).
[51]D. X. Li, Y. Haga, H. Shida, T. Suzuki, and Y. S. Kwon, Phys. Rev. B **54**, 10483 (1996).
[52]H. Taub and S. J. Williamson, Solid State Commun. **13**, 1021 (1973).
[53]J. J. Song, F. Tang, W. Zhou, Y. Fang, H. L. Yu, Z. D. Han, B. Qian, X. F. Jiang, D. H. Wang, and Y. W. Du, J. Mater. Chem. C **6**, 3026 (2018).
[54]S. J. Allen, N. Tabatabaie, C. J. Palmstrøm, G. W. Hull, T. Sands, F. DeRosa, H. L. Gilchrist, and K. C. Garrison, Phys. Rev. Lett. **62**, 2309 (1989).
[55]S. Jang, R. Kealhofer, C. John, S. Doyle, J. Hong, J. H. Shim, Q. Si, O. Erten, J. D. Denlinger, and J. G. Analytis, Sci. Adv. **5**, eaat7158 (2019).
[56]H. Kępa, G. Springholz, T. M. Giebultowicz, K. I. Goldman, C. F. Majkrzak, P. Kacman, J. Blinowski, S. Holl, H. Krenn, and G. Bauer, Phys. Rev. B **68**, 024419 (2003).
[57]B. Biswas and B. Saha, Phys. Rev. Mater. **3**, 020301 (2019).
[58]C. Duan, R. F. Sabiryanov, J. Liu, W. N. Mei, P. A. Dowben, and J. R. Hardy, Phys. Rev. Lett. **94**, 237201 (2005).
[59]W. Al-Sawai, H. Lin, R. S. Markiewicz, L. A. Wray, Y. Xia, S.-Y. Xu, M. Z. Hasan, and A. Bansil, Phys. Rev. B **82**, 125208 (2010).
[60]S. Chadov, X. Qi, J. Kübler, G. H. Fecher, C. Felser, and S. C. Zhang, Nat. Mater. **9**, 541 (2010).
[61]H. Lin, L. A. Wray, Y. Xia, S. Xu, S. Jia, R. J. Cava, A. Bansil, and M. Z. Hasan, Nat. Mater. **9**, 546 (2010).

07 November 2023 07:54:06

© Author(s) 2023